Research Article | Vol. 8, No. 1 | 1 Jan 2017 | BIOMEDICAL OPTICS EXPRESS 112

Biomedical Optics EXPRESS

Deep tissue photoacoustic computed tomography with a fast and compact laser system

DEPENG WANG,[1] YUEHANG WANG,[1] WEIRAN WANG,[2] DANDAN LUO,[1] UPENDRA CHITGUPI,[1] JUMIN GENG,[1] YANG ZHOU,[1,3] LIDAI WANG,[4] JONATHAN F LOVELL,[1] AND JUN XIA[1,*]

[1]*Department of Biomedical Engineering, University at Buffalo, State University of New York, Buffalo, USA*
[2]*Department of Electronic Engineering, City University of Hong Kong, Hong Kong, China*
[3]*College of Chemistry, Chemical Engineering and Materials Science, Collaborative Innovation Center of Functionalized Probes for Chemical Imaging in Universities of Shandong, Key Laboratory of Molecular and Nano Probes, Ministry of Education, Shandong Provincial Key Laboratory of Clean Production of Fine Chemicals, Shandong Normal University, Jinan, China*
[4]*Department of Mechanical and Biomedical Engineering, City University of Hong Kong, Hong Kong, China*
[*]*junxia@buffalo.edu*

Abstract: Photoacoustic computed tomography (PACT) holds great promise for biomedical imaging, but wide-spread implementation is impeded by the bulkiness of flash-lamp-pumped laser systems, which typically weigh between 50 - 200 kg, require continuous water cooling, and operate at a low repetition rate. Here, we demonstrate that compact lasers based on emerging diode technologies are well-suited for preclinical and clinical PACT. The diode-pumped laser used in this study had a miniature footprint ($13 \times 14 \times 7$ cm^3), weighed only 1.6 kg, and outputted up to 80 mJ per pulse at 1064 nm. *In vitro*, the laser system readily provided over 4 cm PACT depth in chicken breast tissue. *In vivo*, in addition to high resolution, non-invasive brain imaging in living mice, the system can operate at 50 Hz, which enabled high-speed cross-sectional imaging of murine cardiac and respiratory function. The system also provided high quality, high-frame rate, and non-invasive three-dimensional mapping of arm, palm, and breast vasculature at multi centimeter depths in living human subjects, demonstrating the clinical viability of compact lasers for PACT.

OCIS codes: (110.0110) Imaging systems; (140.0140) Lasers and laser optics; (110.5120) Photoacoustic imaging.

References and links

1. L. V. Wang and S. Hu, "Photoacoustic tomography: in vivo imaging from organelles to organs," Science **335**(6075), 1458–1462 (2012).
2. D. Wang, Y. Wu, and J. Xia, "Review on photoacoustic imaging of the brain using nanoprobes," Neurophotonics **3**(1), 010901 (2016).
3. H. F. Zhang, K. Maslov, G. Stoica, and L. V. Wang, "Functional photoacoustic microscopy for high-resolution and noninvasive in vivo imaging," Nat. Biotechnol. **24**(7), 848–851 (2006).
4. Y. Jin, C. Jia, S.-W. Huang, M. O'Donnell, and X. Gao, "Multifunctional nanoparticles as coupled contrast agents," Nat. Commun. **1**(4), 41 (2010).
5. J. Yao, L. Wang, J.-M. Yang, K. I. Maslov, T. T. Wong, L. Li, C.-H. Huang, J. Zou, and L. V. Wang, "High-speed label-free functional photoacoustic microscopy of mouse brain in action," Nat. Methods **12**(5), 407–410 (2015).
6. A. P. Jathoul, J. Laufer, O. Ogunlade, B. Treeby, B. Cox, E. Zhang, P. Johnson, A. R. Pizzey, B. Philip, T. Marafioti, M. F. Lythgoe, R. B. Pedley, M. A. Pule, and P. Beard, "Deep in vivo photoacoustic imaging of mammalian tissues using a tyrosinase-based genetic reporter," Nat. Photonics **9**, 239–246 (2015).
7. X. Wang, Y. Pang, G. Ku, X. Xie, G. Stoica, and L. V. Wang, "Noninvasive laser-induced photoacoustic tomography for structural and functional in vivo imaging of the brain," Nat. Biotechnol. **21**(7), 803–806 (2003).
8. J. Xia, M. R. Chatni, K. Maslov, Z. Guo, K. Wang, M. Anastasio, and L. V. Wang, "Whole-body ring-shaped confocal photoacoustic computed tomography of small animals in vivo," J. Biomed. Opt. **17**(5), 050506 (2012).

#278767 http://dx.doi.org/10.1364/BOE.8.000112
Journal © 2017 Received 17 Oct 2016; revised 2 Dec 2016; accepted 4 Dec 2016; published 8 Dec 2016

Biomedical Optics EXPRESS

9. R. A. Kruger, C. M. Kuzmiak, R. B. Lam, D. R. Reinecke, S. P. Del Rio, and D. Steed, "Dedicated 3D photoacoustic breast imaging," Med. Phys. **40**(11), 113301 (2013).
10. A. Garcia-Uribe, T. N. Erpelding, A. Krumholz, H. Ke, K. Maslov, C. Appleton, J. A. Margenthaler, and L. V. Wang, "Dual-Modality Photoacoustic and Ultrasound Imaging System for Noninvasive Sentinel Lymph Node Detection in Patients with Breast Cancer," Sci. Rep. **5**, 15748 (2015).
11. H. Jelínková, *Lasers for Medical Applications: Diagnostics, Therapy and Surgery* (Elsevier, 2013).
12. L. V. Wang and L. Gao, "Photoacoustic microscopy and computed tomography: from bench to bedside," Annu. Rev. Biomed. Eng. **16**(1), 155–185 (2014).
13. K. Sivasubramanian and M. Pramanik, "High frame rate photoacoustic imaging at 7000 frames per second using clinical ultrasound system," Biomed. Opt. Express **7**(2), 312–323 (2016).
14. K. Daoudi, P. J. van den Berg, O. Rabot, A. Kohl, S. Tisserand, P. Brands, and W. Steenbergen, "Handheld probe integrating laser diode and ultrasound transducer array for ultrasound/photoacoustic dual modality imaging," Opt. Express **22**(21), 26365–26374 (2014).
15. T. J. Allen and P. C. Beard, "Pulsed near-infrared laser diode excitation system for biomedical photoacoustic imaging," Opt. Lett. **31**(23), 3462–3464 (2006).
16. R. G. Kolkman, W. Steenbergen, and T. G. van Leeuwen, "In vivo photoacoustic imaging of blood vessels with a pulsed laser diode," Lasers Med. Sci. **21**(3), 134–139 (2006).
17. K. Maslov and L. V. Wang, "Photoacoustic imaging of biological tissue with intensity-modulated continuous-wave laser," J. Biomed. Opt. **13**, 024006 (2008).
18. T. Murray and O. Balogun, "High-sensitivity laser-based acoustic microscopy using a modulated excitation source," Appl. Phys. Lett. **85**(14), 2974–2976 (2004).
19. C.-W. Wei, T.-M. Nguyen, J. Xia, B. Arnal, E. Y. Wong, I. M. Pelivanov, and M. O'Donnell, "Real-time integrated photoacoustic and ultrasound (PAUS) imaging system to guide interventional procedures: ex vivo study," IEEE Trans. Ultrason. Ferroelectr. Freq. Control **62**(2), 319–328 (2015).
20. P. K. Upputuri and M. Pramanik, "Performance characterization of low-cost, high-speed, portable pulsed laser diode photoacoustic tomography (PLD-PAT) system," Biomed. Opt. Express **6**(10), 4118–4129 (2015).
21. A. Buehler, M. Kacprowicz, A. Taruttis, and V. Ntziachristos, "Real-time handheld multispectral optoacoustic imaging," Opt. Lett. **38**(9), 1404–1406 (2013).
22. B. Lashkari, S. S. Sean Choi, M. E. Khosroshahi, E. Dovlo, and A. Mandelis, "Simultaneous dual-wavelength photoacoustic radar imaging using waveform engineering with mismatched frequency modulated excitation," Opt. Lett. **40**(7), 1145–1148 (2015).
23. K. Homan, S. Kim, Y.-S. Chen, B. Wang, S. Mallidi, and S. Emelianov, "Prospects of molecular photoacoustic imaging at 1064 nm wavelength," Opt. Lett. **35**(15), 2663–2665 (2010).
24. Z. ANSI, "136.1 American National Standard for Safe Use of Lasers," Laser Institute of America, Orlando (2000).
25. A. S. Hannah, D. VanderLaan, Y.-S. Chen, and S. Y. Emelianov, "Photoacoustic and ultrasound imaging using dual contrast perfluorocarbon nanodroplets triggered by laser pulses at 1064 nm," Biomed. Opt. Express **5**(9), 3042–3052 (2014).
26. G. Ku, M. Zhou, S. Song, Q. Huang, J. Hazle, and C. Li, "Copper Sulfide Nanoparticles as a New Class of Photoacoustic Contrast Agent for Deep Tissue Imaging at 1064 nm," ACS Nano **6**(8), 7489–7496 (2012).
27. Y. Zhou, D. Wang, Y. Zhang, U. Chitgupi, J. Geng, Y. Wang, Y. Zhang, T. R. Cook, J. Xia, and J. F. Lovell, "A Phosphorus Phthalocyanine Formulation with Intense Absorbance at 1000 nm for Deep Optical Imaging," Theranostics **6**(5), 688–697 (2016).
28. T. Furuyama, K. Satoh, T. Kushiya, and N. Kobayashi, "Design, synthesis, and properties of phthalocyanine complexes with main-group elements showing main absorption and fluorescence beyond 1000 nm," J. Am. Chem. Soc. **136**(2), 765–776 (2014).
29. G. Marquez, L. V. Wang, S.-P. Lin, J. A. Schwartz, and S. L. Thomsen, "Anisotropy in the absorption and scattering spectra of chicken breast tissue," Appl. Opt. **37**(4), 798–804 (1998).
30. J. L. Sandell and T. C. Zhu, "A review of in-vivo optical properties of human tissues and its impact on PDT," J. Biophotonics **4**(11-12), 773–787 (2011).
31. M. Xu and L. V. Wang, "Universal back-projection algorithm for photoacoustic computed tomography," Phys. Rev. E Stat. Nonlin. Soft Matter Phys. **71**(1), 016706 (2005).
32. J. Gamelin, A. Maurudis, A. Aguirre, F. Huang, P. Guo, L. V. Wang, and Q. Zhu, "A real-time photoacoustic tomography system for small animals," Opt. Express **17**(13), 10489–10498 (2009).
33. A. Dima, N. C. Burton, and V. Ntziachristos, "Multispectral optoacoustic tomography at 64, 128, and 256 channels," J. Biomed. Opt. **19**(3), 036021 (2014).
34. A. F. Frangi, W. J. Niessen, K. L. Vincken, and M. A. Viergever, "Multiscale vessel enhancement filtering," in *International Conference on Medical Image Computing and Computer-Assisted Intervention* (Springer, 1998), 130–137.
35. B. E. Treeby and B. T. Cox, "k-Wave: MATLAB toolbox for the simulation and reconstruction of photoacoustic wave fields," J. Biomed. Opt. **15**(2), 021314 (2010).
36. H.-M. Schwab, M. F. Beckmann, and G. Schmitz, "Photoacoustic clutter reduction by inversion of a linear scatter model using plane wave ultrasound measurements," Biomed. Opt. Express **7**(4), 1468–1478 (2016).

Biomedical Optics EXPRESS

37. M. K. A. Singh, M. Jaeger, M. Frenz, and W. Steenbergen, "In vivo demonstration of reflection artifact reduction in photoacoustic imaging using synthetic aperture photoacoustic-guided focused ultrasound (PAFUSion)," Biomed. Opt. Express **7**(8), 2955–2972 (2016).
38. A. J. Ewald, Z. Werb, and M. Egeblad, "Monitoring of vital signs for long-term survival of mice under anesthesia," Cold Spring Harbor protocols **2011**, pdb. prot5563 (2011).
39. D. Wang, Y. Wang, Y. Zhou, J. F. Lovell, and J. Xia, "Coherent-weighted three-dimensional image reconstruction in linear-array-based photoacoustic tomography," Biomed. Opt. Express **7**(5), 1957–1965 (2016).
40. Y. Wang, D. Wang, Y. Zhang, J. Geng, J. F. Lovell, and J. Xia, "Slit-enabled linear-array photoacoustic tomography with near isotropic spatial resolution in three dimensions," Opt. Lett. **41**(1), 127–130 (2016).
41. V. W. Wong, R. D. Katz, and J. P. Higgins, "Interpretation of upper extremity arteriography: vascular anatomy and pathology [corrected]," Hand Clin. **31**(1), 121–134 (2015).
42. B. Christian and J. Upton, "Congenital Vascular Disorders," in *The Pediatric Upper Extremity* (Springer, 2015), pp. 1545–1578.
43. B. P. Schneider and K. D. Miller, "Angiogenesis of breast cancer," J. Clin. Oncol. **23**(8), 1782–1790 (2005).
44. H. Ke, T. N. Erpelding, L. Jankovic, C. Liu, and L. V. Wang, "Performance characterization of an integrated ultrasound, photoacoustic, and thermoacoustic imaging system," J. Biomed. Opt. **17**(5), 056010 (2012).
45. Z. Zha, Z. Deng, Y. Li, C. Li, J. Wang, S. Wang, E. Qu, and Z. Dai, "Biocompatible polypyrrole nanoparticles as a novel organic photoacoustic contrast agent for deep tissue imaging," Nanoscale **5**(10), 4462–4467 (2013).
46. G. Ku and L. V. Wang, "Deeply penetrating photoacoustic tomography in biological tissues enhanced with an optical contrast agent," Opt. Lett. **30**(5), 507–509 (2005).
47. B. Cox, J. G. Laufer, S. R. Arridge, and P. C. Beard, "Quantitative spectroscopic photoacoustic imaging: a review," J. Biomed. Opt. **17**(6), 061202 (2012).
48. A. Hussain, W. Petersen, J. Staley, E. Hondebrink, and W. Steenbergen, "Quantitative blood oxygen saturation imaging using combined photoacoustics and acousto-optics," Opt. Lett. **41**(8), 1720–1723 (2016).
49. L. Wang, J. Xia, J. Yao, K. I. Maslov, and L. V. Wang, "Ultrasonically encoded photoacoustic flowgraphy in biological tissue," Phys. Rev. Lett. **111**(20), 204301 (2013).
50. Y. Zhang, M. Jeon, L. J. Rich, H. Hong, J. Geng, Y. Zhang, S. Shi, T. E. Barnhart, P. Alexandridis, J. D. Huizinga, M. Seshadri, W. Cai, C. Kim, and J. F. Lovell, "Non-invasive multimodal functional imaging of the intestine with frozen micellar naphthalocyanines," Nat. Nanotechnol. **9**(8), 631–638 (2014).
51. A. Danielli, C. P. Favazza, K. Maslov, and L. V. Wang, "Single-wavelength functional photoacoustic microscopy in biological tissue," Opt. Lett. **36**(5), 769–771 (2011).
52. J. Yao, A. A. Kaberniuk, L. Li, D. M. Shcherbakova, R. Zhang, L. Wang, G. Li, V. V. Verkhusha, and L. V. Wang, "Multiscale photoacoustic tomography using reversibly switchable bacterial phytochrome as a near-infrared photochromic probe," Nat. Methods **13**(1), 67–73 (2016).

1. Introduction

Photoacoustic (PA) computed tomography (PACT) has emerged as a novel imaging modality that provides high resolution imaging of optical absorption in deep tissue [1–6]. Over the past few years, various preclinical and clinical applications of the technique have been demonstrated, including functional brain imaging [7], small-animal whole-body imaging [8], breast cancer screening [9], and guidance of lymph node biopsy [10]. To ensure efficient conversion of optical absorption into ultrasound, PACT systems typically utilize high-power nanosecond pulsed laser sources. Most of these lasers are flash-lamp-pumped with output energy ranging from tens to hundreds of millijoules (mJ). Due to the wide emission spectrum of a flash lamp, the conversion efficiency of electrical energy into laser beam energy is very low (1-2%), resulting enormous heat generation. Thus a flash-lamp-based laser requires either open-loop or close-loop water cooling and the system is complicated and bulky [11]. The pulse repetition frequency is also limited (commonly at 10 Hz or 20 Hz) due to the same heating restriction. In addition, the high excitation voltage (several kV) of a flash lamp is unsafe and may cause electrical interferences in a clinical setting. These limitations pose significant barriers to clinical and preclinical translation of the photoacoustic technique [12]. For instance, it can be difficult or impossible to install a photoacoustic instrument at a space-constrained clinical site, thereby impeding the ability to perform studies with clinical subjects. Smaller systems would likely improve the clinical viability of PACT.

Diode pumped lasers can potentially address the aforementioned limitations. Because the emission spectrum of a laser diode is much narrower than a flash lamp, the energy conversion efficiency is much higher (>20%), which significantly simplifies the system design and reduces the size. Over the past few years, several groups have demonstrated the use of diode-pumped lasers for photoacoustic imaging. For instance, Sivasubramanian et al. achieved a

Biomedical Optics EXPRESS

photoacoustic imaging speed of 7000 frames per second, which represents the current world record of high speed PACT [13]. Daoudi et al. developed the first handheld probe that integrates laser diode and ultrasound transducer into a small foot print [14]. However, because of the low pulse energy (less than a few millijoules), a common limitation of diode laser-based systems is the limited penetration depth [15–18]. To circumvent this limitation, Wei et al. proposed to optically scan a narrow beam over a large region for deep tissue imaging [19]. In theory, this approach allows high intensity illumination over a large region. However, in practice, the imaging depth is limited by the system's detection limit at each scanning position: below the noise level, photoacoustic features cannot be coherently reconstructed from signals acquired at different light illumination spots. Therefore, the demonstrated imaging depth in that study was only 12 mm, which is far less than their theoretical estimation. Alternatively, Daoudi et al. [14] and Upputuri et al. [20] expanded the laser beam and tried to improve the imaging depth through averaging. They achieved 15 mm and 20 mm imaging depths, respectively. While these imaging depths could be sufficient for certain clinical applications such as imaging of rheumatoid arthritis and skin cancer, they are not sufficient for imaging solid tumors or brains. Higher power diode laser systems have also been used for deeper imaging depth, however, they either are also bulky and require the same water cooling of a flash-lamp-pumped laser [21] or have low efficiency in photoacoustic signal generation [22].

In this study, we introduce the first use of a compact and high-power laser for deep tissue *in vivo* PACT. The laser, designed by Montfort Laser GmbH, has a miniature size of 13.2 (length) × 14.0 (width) × 6.5 (height) cm, a low weight of 1.6 kg, a good M^2 factor of 3, and a high pulse energy of up to 80 mJ. The pulse repetition frequency of the laser can be tuned from single pulse to 50 Hz for various imaging needs. The output wavelength is fixed at 1064 nm, which is within the near infrared window for deep tissue imaging. Compared to shorter wavelength lights (650~900 nm), the 1064 nm wavelength holds numerous advantages, including low optical scattering, high wall-plug efficiency, homogeneous signal from background tissue [23], good absorption to oxy-hemoglobin, and a high American National Standards Institute (ANSI) [24] safety limit. These advantages have led to active developments of 1064 nm contrast agents for various imaging applications [25–27].

Through phantom and *in vivo* imaging studies, we successfully detected a tube of 1064 nm contrast agent [27] embedded under 4.1 cm chicken breast tissue, imaged murine whole-body vascular structures and cardiac functions *in vivo*, and mapped the arm, palm and breast vasculatures of living human subjects.

2. Methods

2.1 Laser

The Montfort laser (M-NANO-Nd:YAG-10ns-50-INDR_PR135) used in this study [Fig. 1(a)] provides up to 4 W average output power. As mentioned previously, a diode pumped laser is significantly smaller than a flash-lamp-pumped laser. For better comparison, Table 1 summarizes the specifications of the Montfort laser and our flash-lamp-pumped laser (SLIII-10, Continuum, a typical light source for PACT applications). It can be seen that for the laser head, the Montfort laser occupies only 4.5% volume and 6.7% weight of the Continuum laser. As for the power supply, the Montfort laser uses a miniature AC to DC converter (100-240 VAC to 24-28 VDC), while the Continuum laser requires 200~240 VAC input and the power supply has a built-in high voltage converter and water tank, resulting in heavy weight and bulky size. Thus, the compact laser could easily overcome the space-constrained problems faced by the flash-lamp lasers, providing great flexibility for different imaging applications. In addition, the pulse repetition rate of the compact laser ranges from single pulse to 50 Hz, while the Continuum laser operates at a fixed 10 Hz repetition rate. The pulse energy of the Continuum laser is indeed higher than the compact laser. However, the increase in energy is

Biomedical Optics EXPRESS

small compared to the added weight and volume. As will be seen in the results section, sub 100 mJ output is sufficient for most preclinical and clinical imaging applications.

To identify the optimum pulse repetition rate for imaging, we measured the maximum pulse energy at eight different pulse repetition frequencies. Because the total laser output power is limited at 4 W, increasing the pulse repetition rate leads to a decrease in pulse energy [Fig. 1(b)]. Beyond 50 Hz, the output energy dropped very quickly and passive air cooling was not sufficient for prolonged laser operation. Thus, in this study we operated the laser at only 10 to 50 Hz. A major limitation of diode-pumped laser is the relatively poor beam quality. Fig. 1(c) shows a photograph of laser beam profiles acquired with a burn paper placed 7 cm away from the output window. The beam has an irregular shape which may cause issues when tight optical focusing is needed. Fortunately, PACT relies on diffused photons to form an image and the beam quality is less critical. To ensure uniform coupling of laser output into an optical fiber bundle, we placed an engineered diffuser at a distance 3.5 cm away from the output window (EDS-20-A-1s, RPC Photonics). As shown in Fig. 1(c), the diffused beam has a circular profile (measured 3.5 cm away from the diffuser) and can be readily coupled into the circular input of optical fiber bundle.

Table 1. Comparison of compact laser and the Nd:YAG laser

Type		Continuum (C)	Montfort (M)	Ratio (M/C)
Size	Laser head	77.5 × 17.8 × 19.0 cm^3	13.2 × 14.0 × 6.5 cm^3	4.5%
	Power supply	62.2 × 28.2 × 50.8 cm^3	19.0 × 8.5 × 5.3 cm^3	0.9%
Weight (kg)	Laser head	24.0	1.6	6.7%
	Power supply	44.0	0.8	1.8%
Operation voltage range of power supply		110~240 V AC	200~240 VAC	—
Pulse repetition frequency (Hz)		10 Hz	Single pulse to 50 Hz	—
Max energy per pulse (mJ)		850	80~50 (10~50 Hz)	9.4%~5.9%

2.2 Penetration depth of PACT system using the compact laser

To quantify the imaging depth of our compact-laser-based PACT system, we imaged a tube filled with 1064 nm contrast agent [27]. The experimental procedure is similar to the one mentioned in [27], which holds the current world record of PACT imaging depth (11.6 cm). The phantom was made of a 5-mm-inner-diameter Tygon tube filled with 30 mM (solvent is Tween 80) phosphorus phthalocyanine (P-Pc) [27, 28], an organic dye with strong absorption at 1064 nm (absorption coefficient is 1.02 × 10^3 cm^{-1}at 1064 nm). The experiment was performed in a 500 mL beaker. The bottom of beaker was covered with 5-cm-thickness chicken breast tissues [Fig. 1(d)], whose optical properties is comparable to that of human breast [29, 30]. The tube was placed on top of the tissue, and during the experiment we gradually stacked chicken breast tissues on top of the tube.

Output from the laser was routed to the top surface of chicken breast tissue through a 1.2 cm diameter circular fiber bundle (#39-371, Edmund Optics, ~50% coupling efficiency). To ensure maximum pulse energy, we used 10 Hz pulse repetition rate. Light intensity over the 1.5-cm-diameter illuminated region was around 22 mJ/cm^2, which is below the ANSI safety limitation at 1064 nm (100 mJ/cm^2) [24]. PA signal of the tube was acquired by a 128-element clinical liner transducer array (ATL/Philips L7-4) with 5 MHz central frequency. The received PA signals were amplified (by 54 dB) and digitized by a 128-channel ultrasound data acquisition (DAQ) system (Vantage, Verasonics) with 20 MHz sampling rate. After each laser pulse, the raw channel data was reconstructed using the universal back-projection algorithm [31], and was displayed in real-time during experiments.

2.3 Mice imaging

Pre-clinical imaging performance of the compact laser was demonstrated through whole-body imaging of mice. For brain imaging, because the cortex is only approximately 1 mm beneath the scalp surface, we used top illumination [Fig. 1(e)]. The laser light was delivered to the

Biomedical Optics EXPRESS

brain through the 1.2 cm diameter fiber bundle. The maximum light intensity at the skin surface was around 12 mJ/cm^2, which is below the ANSI safety limitation [24] of 100 mJ/cm^2. For trunk imaging, the animal was immersed in water and light delivery was provided by a 6-cm-diameter ring fiber illuminator (Light Source Flex Cable 12-Light Ring-Mount, Fiberoptic Specialties) [Fig. 2(f)]. Along the ring, twelve circular fiber outputs (0.3 cm in diameter) are evenly distributed and are all illuminating toward the ring center at a 60° angle (along the elevation direction). During the experiment, we adjusted the height of the ring fiber to ensure that the imaged cross section receives the maximum light energy. To image different body cross sections, the animal can be translated along elevation through a motorized translation stage.

The photoacoustic signals were detected by a custom-made three-quarter ring transducer array with 128 elements and 5 MHz central frequency. The radius of the ring array was 40 mm and each element forms an elevation focus at 35 mm. Thus elevation resolution and receiving sensitivity are relatively uniform at the central 10 mm radius region [marked as the field of view (FOV) in Fig. 2(g)] [32, 33]. For both brain and trunk imaging, we used heat lamp to keep the mouse warm and we ensured that the area of interest was within the FOV. Signals from the transducer array were transmitted to the Vantage system through custom-made cables and connectors. Brain, liver and kidney regions were all imaged with 10 Hz pulse repetition frequency over 50 seconds, while the heart region was imaged with 50 Hz pulse repetition frequency over 10 seconds. With matched number of DAQ channels and transducer elements, a cross sectional image can be acquired after each laser pulse. The raw data was reconstructed with the universal back-projection algorithm [31], and processed through a vessel enhancement filter to highlight the blood vessels [34]. For visualizations in the supplementary file, we did not apply the vessel enhancement filter and did not perform any signal averaging.

2.4 Human imaging

The right arm and left palm of two male volunteers, and the right breast (B cup) of a female volunteer were imaged with the compact laser. All the experiments were performed in compliance with the University at Buffalo IRB protocol. Light delivery was provided by a bifurcated fiber bundle (SCHOTT Inc.) with a 1-cm-diameter circular input and two 5-cm-length line outputs. For photoacoustic detection, we used an ATL/Philips L7-4 liner transducer array. As shown in Fig. 2(h), both the L7-4 array head and the fiber outputs were immersed in water while the object (palm, arm or breast) was positioned underneath the water tank and coupled with ultrasound gel. During imaging, the transducer and fiber bundles moved simultaneously while the object stayed stationary. To ensure good elevation resolution, the object was placed at the elevation focus of the transducer array (25 mm axial distance).

For arm and palm experiments, we used 50 Hz pulse repetition frequency. The excited area at the skin surface was around 5 cm by 1 cm in size and the maximum light intensity was 8 mJ/cm^2, which is also far below the ANSI limit. To scan a 40 mm length, the experiment took 8 seconds, generating 400 two-dimensional (2D) data sets. For breast imaging, we used 10 Hz pulse repetition frequency in order to get the maximum pulse energy. The light intensity was around 14 mJ/cm^2, which is still below the safety limit. During the experiment, transducer and fiber bundles scanned over a 75 mm region at a speed of 1 mm/s. For all human experiments, the raw-channel data was first filtered with a band-pass filter (5~8 MHz) and then reconstructed with the back-projection algorithm [31]. Stacking 2D reconstructed images along elevation formed a three-dimensional (3D) image of the object.

Biomedical Optics EXPRESS

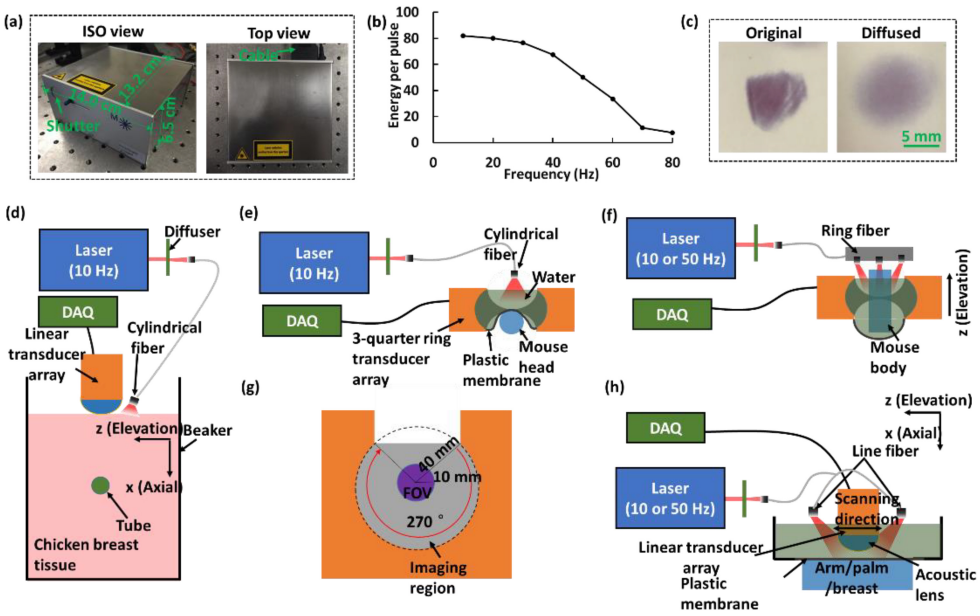

Fig. 1. Compact laser and photoacoustic setups used in phantom, animal and human imaging studies. (a). Photographs of the diode-pumped Nd:YAG laser. (b) Maximum pulse energy at different pulse repetition frequencies. (c) The original laser beam profile and the homogenized laser beam profile. (d) Schematic drawing of the setup used for tube phantom experiment, DAQ: data acquisition. (e) Schematic drawing of the setup used for mouse brain imaging. (f) Schematic drawing of the setup used for trunk imaging. (g) Top view of the three-quarter ring transducer array, FOV: field of view. (h) Schematic drawing of the set up used for human imaging.

3. Results

3.1 Phantom experiment with chicken breast tissue

To quantify the imaging depth, we gradually stacked chicken breast tissues on top of the tube [Fig. 2(a)] and monitored the photoacoustic signal in real time. As the tissue thickness increased, the tube's signal decreased and was eventually buried in background noise (without averaging) when the depth reached approximately 4 cm (measured with a ruler). We then stopped stacking chicken breast tissue and considered this distance as the deepest detection depth. One hundred frames were acquired at this depth, and all data were averaged to improve signal to noise ratio (SNR). The corresponding overlaid photoacoustic (color scale) and ultrasound (gray scale) image is shown in Fig. 2(b), in which the tube is clearly visible with 18 dB SNR. Distance from tube to the transducer surface was calculated to be 4.1 cm, which is 2.1 times deeper than what was demonstrated in the previous compact-laser-based photoacoustic system (2.0 cm) [20]. Considering 50% energy loss through fiber coupling, the imaging depth could be even higher if we use fused silica optical fiber bundles (up to 80% coupling efficiency) or free-space light illumination. After one hundred times averaging, the SNR at different imaging depths was quantified using the following formula: $\mathrm{SNR} = 20log_{10}(\frac{\mu}{\sigma})$, where μ represents the mean values of signal within box 1 and σ is the standard deviation of signal within box 2 (a region contain mainly background signal). The quantified SNR is shown in Fig. 2(c). As expected, the value decreases as the depth increases. This experiment clearly proved the deep-tissue imaging capability of the compact laser.

Biomedical Optics EXPRESS

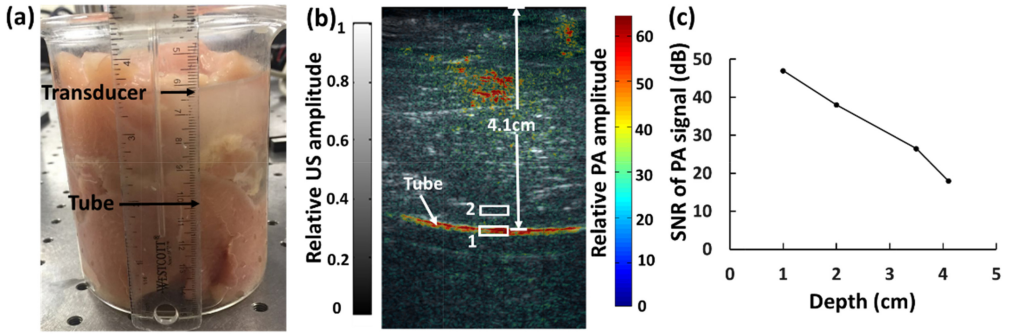

Fig. 2. Chicken breast tissue experiment. (a) Photograph of the tube phantom experiment. (b) Overlaid averaged photoacoustic (color scale) and ultrasound (gray scale) images of the contrast-containing tube at 4.1 cm depth. (c) SNR of photoacoustic signals of the tube at different depths.

3.2 Whole-body imaging of mice

Mice were imaged based on the endogenous hemoglobin contrast. For brain imaging, *in vivo* cortical vascular was imaged through intact scalp. To improve the SNR, we averaged 10 frames without significant head movement. The averaged image [Fig. 3(a)] clearly shows major cortical vessels, including the inferior cerebral vein (ICV), superior sagittal sinus (SSS), transverse sinus (TS), and confluence of sinuses (Cos). Small cortical vessels [labeled as 1 in Fig. 3(a)] could also be seen in both hemispheres, with decreased intensities.

For trunk imaging, the corresponding cross sections of heart, liver and kidneys are shown in Figs. 3(b)-3(d), respectively. It can be seen that from the heart region to the kidney region, the cross section diameter gradually increases, which is expected for mouse in the upright position. To improve the cross sectional image of heart region [Fig. 3(b)], 10 frames [labeled with red arrows in Fig. 3(g)] at similar cardiac and respiratory phases were averaged. Because heart is located at the same height of lung, an organ filled with air pockets, blood vessels of the inner heart could not be fully visualized in Fig. 3(b). However, the image can potentially be improved either by algorithms that account for acoustic reflection at air/tissue interfaces [35, 36], or by the photoacoustic-guided focused ultrasound to identify and reduce reflection artifacts [37]. We also averaged 10 frames without significant respiratory motions to produce a clearer contrast to contour of blood rich organs and vascular structures in the liver [Fig. 3(c)] and kidney [Fig. 3(d)] regions.

We also used the system for functional cardiac imaging at 50 Hz frame rate. Visualization 1 shows images acquired over 10 seconds without averaging. Cardiac and respiratory motions can be clearly seen in the Visualization. To quantify the motions, we extracted PA signals along a red line, which goes across the heart region and ribcage in Fig. 3(b). Then, analogous to M-mode ultrasound, we sequentially stacked the one dimensional PA signals of all the frames to form an M-mode PA image [Fig. 3(e)]. In that image, small vibrations (arrow 1) were caused by heartbeat while large vibrations (arrow 2) were caused by respiration. To quantify the rate of the two motions, we tracked the positions of rib cage and heart wall over time [Figs. 3(f) and 3(g)]. Within the 10 seconds time window, two peaks were identified in Fig. 3(f) while 43 peaks were identified in Fig. 3(g), indicating approximately 0.2 Hz respiration rate and 4.3 Hz heartbeat rate, which were expected for mice under deep anesthesia [38]. These results clearly prove the high-speed dynamic imaging capacity of the compact laser.

Biomedical Optics EXPRESS

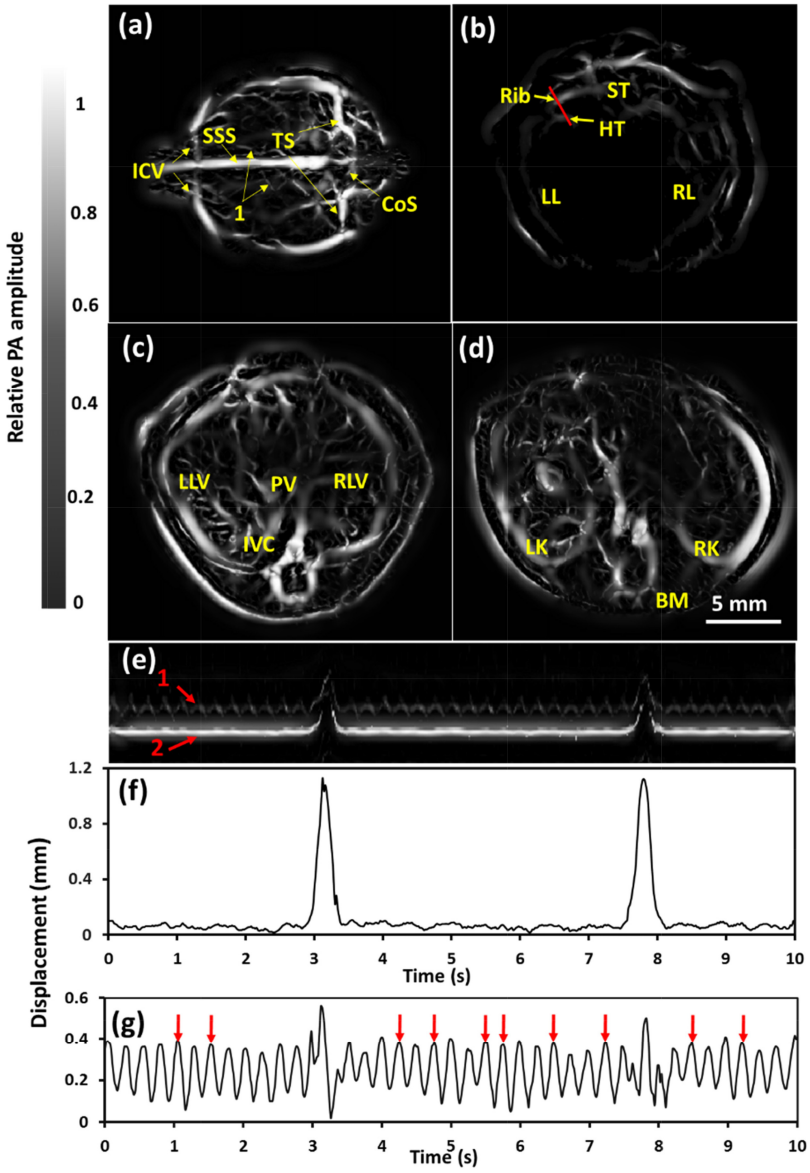

Fig. 3. Mouse anatomical and functional imaging. (a) PA image of cerebral vasculature of a mouse brain. CoS, confluence of sinuses; ICV, inferior cerebral vein; SSS, superior sagittal sinus; TS, transverse sinus. (b) PA cross sectional image of the heart region (Visualization 1). ST, sternum; HT, heart; LL, left lung; RR, right lung. (c) PA cross sectional image of the liver region (Visualization 2). LLV, left lobe of liver; PV, portal vein; RLV, right lobe of liver; IVC, inferior vena cava. (d) PA cross sectional image of the kidney region (Visualization 3). RK, right kidney; LK, left kidney; BM, backbone muscles. (e) M-mode photoacoustic image of cardiac and respiratory motion. (f) Movement of ribcage. (g) Movement of heart wall. Frames at the peaks labeled with red arrows were averaged to improve SNR of Fig. 3(b). Mice: female Swiss Webster, 21 g.

3.3 Human imaging

To demonstrate the feasibility of the laser for human vascular imaging, we first imaged the right arm and left palm of two healthy male volunteers, respectively. With 50 Hz pulse repetition frequency, each 40-mm scan took 8 seconds, which was only one fifth of the

Biomedical Optics EXPRESS

imaging time mentioned in our previous study [39]. Photographs of the arm and palm are shown in Figs. 4(a) and 4(c), respectively. Due to light scattering, blood vessels are not visible in these photographs. In contrast, photoacoustic images in Figs. 4(b) and 4(d) clearly show blood vessels within the imaging region [red dashed box in Figs. 4(a) and 4(c)]. As expected, vascular distribution in the arm is much sparser than that of the palm. Along the white lines in Figs. 4(b) and 4(d), we quantified the elevation resolution to be 1.4 mm and 1.5 mm, respectively. These numbers are close to the elevation resolution (1.5 mm) of the transducer at the acoustic focus. We also quantified the SNR of both images using the selected signals [box 1 in Fig. 4(b) and box 3 in Fig. 4(d)] and noises [box 2 in Fig. 4(b) and box 4 in Fig. 4(b)]. The SNR was 39 dB for Fig. 4(b) and 36 dB for Fig. 4(d).

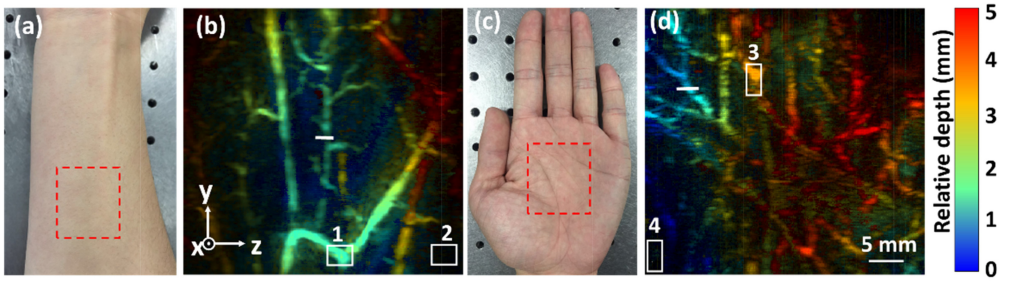

Fig. 4. *In vivo* arm and palm imaging of healthy human volunteers. (a) Photograph of human arm (red box indicates the imaged region). Subject: male, 25 years old. (b) Depth-encoded maximum amplitude projection (MAP) photoacoustic image of the human arm (Visualization 4). x, y and z correspond to axial, lateral and elevation directions of the transducer array, respectively. MAP was performed along the axial direction. (c) Photograph of human palm (red box indicates the imaging region). Subject: male, 23 years old. (d) Depth-encoded MAP photoacoustic image of human palm (Visualization 5), MAP was performed along the axial direction of transducer array

We also imaged the right breast of a female volunteer. As shown in Fig. 5(a), the subject laid supine on a patient bed and the imaging probe was placed on top of the breast. Ultrasound gel was applied as the coupling medium between breast and the imaging window. Figure 5(b) shows the depth-encoded result without averaging, where blood vessels are clearly visible at different depths. Using the signal within box 1 and the noise within box 2 in Fig. 5(b), we quantified the SNR to be 36 dB. The elevation resolution was also quantified (along the white line) to be 1.5 mm. In this pilot study, we imaged up to 15 mm depth, which is less than the P-Pc detection depth in chicken breast tissue. The shallower depth can be attributed to the low absorption coefficient of human blood, the small breast size (B cup and compressed toward the chest wall), and the low light fluence at the skin surface (14 mJ/cm^2). In future studies, we can use a fiber bundle with better coupling efficiency (the current fiber can only couple 50% of light) and perform averaging through respiratory and cardiac gating to improve the imaging depth. Also, because most blood vessels were located within 15 mm of axial depths, we did not use any additional reconstruction methods to further improve the spatial resolution nor contrast ratio. For deep tissue imaging (> 30 mm), we could use our slit-base PACT [40] or coherent-weighted 3D reconstruction [39] to improve the image quality. It should also be noted that our current field of view is limited by the small lateral dimension of the transducer array (38 mm for L7-4). Utilizing a transducer array with a wider lateral dimension, we could potentially image the entire breast at the same imaging speed. This experiment together with the arm and palm experiments clearly demonstrate the clinical imaging capability of the compact laser, indicating its potential in screening upper extremity vascular disorders [41, 42] and breast cancer [43].

Biomedical Optics EXPRESS

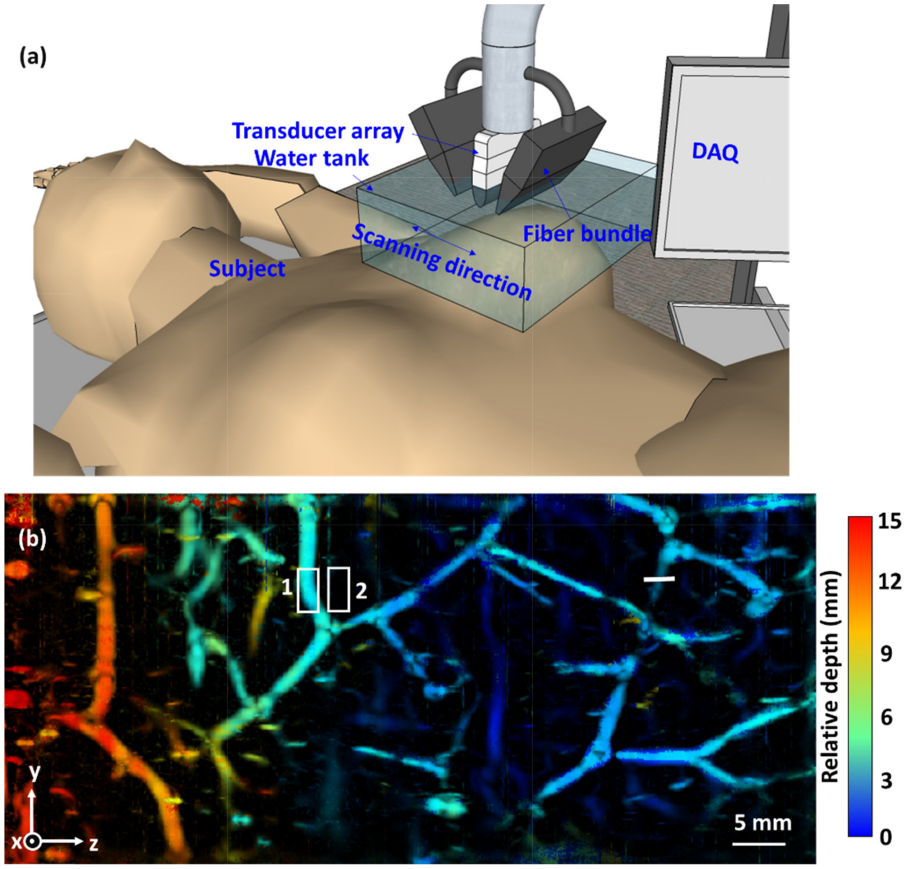

Fig. 5. Breast imaging setup and result. (a) Schematic drawing of the breast imaging setup. (b) Depth-encoded MAP photoacoustic image of breast vasculature in a healthy human volunteer (Visualization 6). Subject: female, 23 years old. x, y and z correspond to axial, lateral and elevation directions the transducer, respectively. MAP was performed along the axial direction of transducer array.

Our results demonstrate that a compact laser approach is well suited for PACT applications. By using a 1064 nm contrast agent, the laser provided an imaging depth of 4.1 cm. This result represents the first over 4 cm photoacoustic imaging using a portable light source [27, 44–46]. The compact laser can also be applied for *in vivo* animal and human imaging. Compared to flash-lamp-pumped lasers, the compact laser can be easily transported between clinics or operation rooms, and it poses minimal electrical interfaces to other medical devices; these can hardly be achieved by a flash-lamp-pumped laser. A limitation of the laser is the fixed output wavelength, which may preclude certain functional and molecular imaging applications, where spectral separation of photoacoustic signals are needed. However, spectral separation requires quantification of local fluence at each wavelength, which itself is challenging in deep tissue [47] and has only been partially addressed recently through acoustic-optics [48]. Nevertheless, our laser output is sufficient to pump an optical parametric oscillator and can potentially achieve multi-wavelength imaging. In addition, single-wavelength-based functional and molecular imaging approaches have shown promise for various applications. For instance, for functional imaging, the blood flow can be quantified based on thermal tagging of red blood cells [49], the intestinal motility can be imaged with contrast agents [50], and the blood oxygenation can be obtained through the saturation-based PA imaging [51]. For molecular imaging, magnetomotive PA [4] and photo-switchable contrast-enhanced PA [52] allow accurate separation of contrast signals with minimum

Biomedical Optics EXPRESS

interference from background. All these techniques can potentially be applied to the compact laser system to achieve anatomical, functional and molecular imaging with single wavelength. Currently, the portability of our PACT system is limited by the relatively larger DAQ system (size of a desktop workstation). However, integration with compact ultrasound research systems is feasible. More compact systems are expected to expand the use of PACT and open up research avenues for applications such as bedside clinical imaging, benchtop lab imaging, emergency medicine and mobile healthcare.

Funding

This work was sponsored in part by University at Buffalo startup funding, the IMPACT Award, the SUNY Brain Network of Excellence Big Idea Award, National Institutes of Health (NIH) (R21EY026411 and DP5OD017898 (J.F.L.)), and the National Natural Science Foundation of China (NSFC) (No. 21401118) (Y.Z.).

Acknowledgment

The authors declare no competing financial interests.